Molecular basis for two stereoselective Diels-Alderases that produce decalin skeletons

Keisuke Fujiyama[1,11], Naoki Kato[2,3,11]*, Suyong Re[4,5], Kiyomi Kinugasa[2], Kohei Watanabe[6], Ryo Takita[6], Toshihiko Nogawa[7], Tomoya Hino[1,10], Hiroyuki Osada[7], Yuji Sugita[4,8,9], Shunji Takahashi[2]*, and Shingo Nagano[1,10]*

[1] Department of Chemistry and Biotechnology, Graduate School of Engineering, Tottori University, Tottori, Japan.
[2] Natural Product Biosynthesis Research Unit, RIKEN Center for Sustainable Research Science, Wako, Japan.
[3] Faculty of Agriculture, Setsunan University, Hirakata, Japan.
[4] Laboratory for Biomolecular Function Simulation, RIKEN Center for Biosystems Dynamics Research, Kobe, Japan.
[5] Center for Drug Design Research, National Institutes of Biomedical Innovation, Health, and Nutrition, Ibaraki, Japan.
[6] Graduate School of Pharmaceutical Sciences, The University of Tokyo, Tokyo, Japan.
[7] Chemical Biology Research Group, RIKEN Center for Sustainable Research Science, Wako, Japan.
[8] Theoretical Molecular Science Laboratory, RIKEN Cluster for Pioneering Research, Wako, Japan.
[9] Computational Biophysics Research Team, RIKEN Center for Computational Science, Kobe, Japan.
[10] Centre for Research on Green Sustainable Chemistry, Tottori University, Tottori, Japan.
[11] These authors contributed equally to this work.

*To whom correspondence should be addressed:
naoki.kato@setsunan.ac.jp; shunjitaka@riken.jp; snagano@tottori-u.ac.jp

Abstract

Enzymes catalyzing [4+2] cycloadditions are involved in the formation of complex structures found in natural products, and play key roles in the control of stereochemistry. Fsa2 and Phm7 catalyze intramolecular [4+2] cycloaddition to form enantiomeric decalin scaffolds during the biosynthesis of HIV-1 integrase inhibitors, equisetin, and an opposite stereochemical homolog, phomasetin. Here, we solved the X-ray crystal structures of substrate-free Fsa2 and Phm7, and an inhibitor-bound Phm7 to understand the molecular basis underlying stereoselective cycloaddition reactions. Based on the crystal structures, docking simulations followed by all-atom molecular dynamics simulations provided binding models demonstrating the folding of linear polyenoyl tetramic acid substrates in the binding pocket of these enzymes, which explain the stereoselectivity in the construction of decalin scaffolds. Site-directed mutagenesis studies verified the binding models and, in combination with density functional theory calculations, clarified how hydrophilic amino acid residues in the Phm7 pocket regulate and catalyze the stereoselective cycloaddition. This powerful combination of experimental and theoretical approaches highlights the distinct molecular mechanisms of enzyme-mediated [4+2] cycloaddition and its stereoselectivity.

Introduction

Molecular chirality, which was discovered by Louis Pasteur in the middle of the 19th century[1], which is observed in primary and secondary metabolites. These biomolecules, particularly secondary metabolites or natural products, are rich in chiral centers (i.e., asymmetric carbon atoms), and the stereochemistry of chiral centers is closely related to their biological functions. Enzymes that create complex carbon frameworks with multiple chiral centers, such as polyketide synthase (PKS) and terpene cyclase, are gaining increasing attention not only in natural product chemistry but also in the chemical industry. Enzymes catalyzing the [4+2] cycloadditions, so-called Diels-Alderases (DAases), form two C-C bonds and up to four chiral centers from conjugated diene and substituted alkene to form a cyclohexene, and play key roles in controlling stereochemistry during the formation of polycyclic structures (Supplementary Fig. 1)[2-5]. Since the discovery of SpnF, which was first reported to catalyze a [4+2] cycloaddition alone[6], many DAases have been identified in the biosynthetic pathways of bacterial, fungal, and plant origins over the past decade. Unlike PKSs and terpene cyclases, which share their active site-containing domain structures for their own functions[7,8], DAases have no common structural features and are derived from distinct progenitor enzymes or proteins. SpnF, which catalyzes [4+2] cycloaddition in the spinosyn A biosynthesis[6], contains *S*-adenosylmethionine (SAM) and its overall structure belongs to the SAM-dependent methyltransferase family[9], and the overall structure of PyrE3, which is a DAase involved in the biosynthesis of pyrroindomycins[10], is very similar to that of FAD-dependent monooxygenases[11]. Although DAases are involved in the stereoselective production of natural products with important biological activities, the molecular basis of this emerging group of enzymes, such as the origin of stereoselectivity and their perfomance as catalysts, has remained elusive.

Fsa2-family decalin synthases (DSs) found in filamentous fungi[12] catalyze stereoselective [4+2] cycloaddition during the biosynthesis of decalin-containing pyrrolidin-2-ones (DPs), which exhibit various biological activities[13,14], including HIV-1 integrase inhibitor equisetin (**1**) and phomasetin (**2**)[15,16] and telomerase inhibitor UCS1025A[17,18] (Fig. 1a). Fsa2 and Phm7 create a decalin scaffold with enantiomeric configurations from similar linear polyenoyl tetramic acids (e.g., **3** and **4**) via intramolecular [4+2] cycloaddition (Fig.1b)[12,19,20]. We have shown that the replacement of *phm7* in **2**-producing fungus with *fsa2* resulted in the production of a **1**-type decalin scaffold (2*S*,3*R*,8*S*,11*R*)[19], indicating that these enzymes determine the stereochemistry of the decalin scaffold during DP biosynthesis. Another homologous enzyme, MycB[21], also produces a **1**-type decalin scaffold, and the **2**-type decalin scaffold is produced by CghA[22] and UcsH[23]. Interestingly, but not surprisingly, it was reported that another decalin scaffold (2*R*,3*S*,8*S*,11*R*) was produced by PvhB involved in the varicidin A biosynthesis[24] (Fig. 1a). Therefore, structural comparisons of the DSs that differ in function, i.e., stereochemical output, provide insight into the mechanisms of the stereoselective [4+2] cycloadditions.

In this study, we demonstrated a molecular basis for two stereoselective enzymes, Fsa2 and Phm7, that catalyze [4+2] cycloaddition to form enantiomeric decalin scaffolds. X-ray crystal structures of substrate-free Fsa2 and Phm7, and Phm7 bound to an inhibitor (hereafter referred to as inhibitor-bound Phm7), were determined at 1.62, 2.17, and 1.61-Å resolution, respectively. The ligand-bound poses were proposed using docking simulations followed by all-atom molecular dynamics (MD) simulations. We employed the generalized replica-exchange with solute tempering (gREST) method[25], which allows binding pose prediction with extensive sampling of multiple possible poses of the substrates[26,27]. Site-directed mutagenesis studies were performed to verify the binding models for the

stereoselective synthesis and examine the amino acid residues involved in the substrate interactions. Density functional theory (DFT) calculations were performed to unveil the reaction mechanism in detail, particularly the stereoselectivity and rate acceleration by Phm7. This powerful combination of experiment methods and calculations to investigate the two enzymes that produce enantiomeric decalin scaffolds provides insight into the molecular mechanism of enzyme-mediated [4+2] cycloaddition and its stereoselectivity.

Results

Structure analyses of Fsa2, Phm7, and inhibitor-bound Phm7

The crystal structure of Fsa2, which produces the 2*S*,3*R*,8*S*,11*R* decalin scaffold found in equisetin (**1**, Fig. 1a,b), has a β-sandwich and a β-barrel domain at the N- and C-termini, respectively (Fig. 2a), and the structures of both domains exhibit structural similarity with those of lipocalin protein family members that bind heme, steroids, and other hydrophobic ligands in the pocket located inside their β structures[28]. Interestingly, however, Fsa2 did not have a pocket inside both the N- and C-domains (Supplementary Fig. 2). Instead, a large pocket was found between the two domains. Considering the plausible substrate structure and volume, the large cavity created by the two domains is very likely to be an active- and substrate-binding site. Phm7 catalyzes intramolecular [4+2] cycloaddition to produce the enantiomeric decalin scaffold (Fig. 1b). Despite their distinct stereoselectivity and low sequence similarity (36% sequence identity), the crystal structure of Phm7 is very similar to that of Fsa2 (RMSD = 0.849 Å), and the shape and volume of the large pocket are very similar for these enzymes (Fig. 2b).

To probe the active site of the DSs, Phm7 ligand screening was carried out using microscale thermophoresis (MST)[29] (Supplementary Fig. 3). We found that 3-aminomethyl-

p-menthane (**5**), which was similar to phomasetin (**2**) substructure, dose-dependently inhibited Phm7 activity *in vitro* and **2** production in a producer fungus, *Pyrenochaetopsis* sp. RK10-F058 (Supplementary Fig. 4). Compound **5** was also confirmed to inhibit equisetin (**1**) production in a producer fungus, *Fusarium* sp. FN080326 (Supplementary Fig. 5). We next performed co-crystallization of Phm7 and **5**, and obtained the crystal structure of the inhibitor-bound Phm7 at 1.61-Å resolution (Supplementary Fig. 6). The inhibitor was located on the lower side of the pocket and formed hydrophobic interactions with Y178, W223, F226, L245, and L381. The amino group of **5** was surrounded by Y68, E51, and Y178. Because **5** can bind to both Phm7 and Fsa2 to inhibit their functions (Supplementary Figs. 3–5), the lower side of the pocket between the two domains would formthe active site of these enzymes. Indeed, a Phm7 homolog, CghA, which is involved in Sch 210972 biosynthesis and exhibits the same stereoselectivity as Phm7 (Fig.1)[22], has two β domains as found for Phm7 and Fsa2; additionally, its product binds to the almost the same position of the **5**-binding site in the pocket between the two domains of CghA (PDB accession codes 6KAW and 6KBC). Therefore, the large pocket found in Phm7 and Fsa2 would constitute the active- and substrate-binding site of cycloadditions by these enzymes.

Docking and MD simulations for binding pose determination

To examine if the pocket would be sufficiently large for accommodating the substrates, substrate **4** was docked into the crystal structure of the inhibitor-bound form of Phm7 using AutoDock Vina[30]. The substrate **4** was found to fit the pocket in various binding poses including a folded form, in which a “U”-shaped folded alkyl chain including asymmetric C6 of **4** was located at the lower side of the pocket where **5** can bind, and the tetramic acid and polyene moieties were extended into the inner upper part of the pocket (Supplementary

Fig. 7a). Likewise, folded substrate **3** was found to fit in the pocket of Fsa2 (Supplementary Fig, 7b). These docking simulations using the crystal structures indicated that the pocket between the N- and C-domains of Phm7 and Fsa2 has enough room for binding of the folded substrates.

The docking results were further refined using all-atom MD simulations using the gREST method[25], which extensively samples multiple possible binding poses otherwise elusive in conventional simulations. A variety of poses were obtained (Supplementary Movies S1 and S2), and clustering analysis of the simulation trajectories resulted in four major bound conformations of **4** and **3**, including “folded” and “extended” conformations (Supplementary Fig. 8). In Fig. 3a, the major cluster of Phm7 (63% of Phm7, pA in Supplementary Fig. 8a) shows a well-defined bound pose for **4**. In this cluster, the tetramic acid moiety of the folded poses was located at the upper front of the pocket and the “U”-shaped part was found at the lower side of the pocket, while the polyene tail was found at the upper back of the pocket. Similar tetramic acid-front and polyene-back poses were also found in the folded ensemble in Fsa2 (33% of Fsa2, fA in Supplementary Fig. 8b), although bound **3** largely fluctuated in the pocket compared to that in Phm7 (Fig. 3b). In both Phm7 and Fsa2, the electrostatic potential inside the pocket showed a large negative value as it moved deeper into the pocket (Supplementary Fig. 9). The bottom surface of the pocket is significantly hydrophobic, while a hydrophilic surface is found at the upper wall of the pocket (Supplementary Fig. 10). These inhomogeneous electrostatic, hydrophobic, and hydrophilic environments of the pocket coincide with the common tetramic acid-front and polyene-back orientation.

The conformation of the central structure of the “folded” cluster of **4** in Phm7 can explain the configuration of the stereoselective [4+2] cycloadduct with the 2*R*,3*S*,8*R*,11*S*

decalin scaffold (Fig. 3c), and many similar poses were also found in the ensemble. LigPlot analysis[31] of the representative pose shows that the tetramic acid moiety forms hydrogen bonds with the side chains of E51, N84, and K356 and with the main chain carbonyl of G64. The U-shaped part and polyene-tail of the substrates were fitted onto the hydrophobic region of the pocket lined by L49, W223, Y232, L245, F341, W342, L381, and I383 (Supplementary Fig. 11a). Several poses in the folded cluster of **3** in Fsa2 are consistent with the configuration of the **1**-type (2*S*,3*R*,8*S*,11*R*) decalin scaffold (Fig. 3c). The hydrophobic U-shaped part and polyene-tail are also surrounded by many hydrophobic side chains (W45, V169, Y171, W216, Y225, and M238), and the tetramic acid moiety is hydrogen bonded with N346 (Supplementary Fig. 11b). Close inspection of the poses revealed that the diene and dienophile moieties of the substrates are pseudo-enantiomeric conformations, which is consistent with the stereochemical relationship of the decalin scaffolds between **1** and **2** (Fig. 3c, Supplementary Fig. 12). Therefore, MD simulations based on the crystal structures of the two enzymes proposed distinct substrate-enzyme interactions and their consequent substrate poses corresponding to the enantiomeric decalin scaffolds.

Functional analyses of Phm7 and Fsa2

To examine the substrate-enzyme interactions predicted from the MD simulations, we first established an *in vitro* enzyme assay system using cell lysates prepared from fungal mycelia lacking the *phm7* gene[19]. The cell lysates were directly incubated with Phm7 or Fsa2, and their reaction products were analyzed by liquid chromatography/electrospray ionization mass spectrometry (LC/ESI-MS). Linear polyenoyl tetramic acid **4** was decreased in the presence of the enzymes, and the expected products of Phm7 and Fsa2,

N-demethylphomasetin (**6**) and its derivative containing **1**-type *trans*-decalin (**7**), respectively, were formed (Fig. 4a,b). The reaction selectivity of Phm7 and Fsa2 shown in the *in vitro* assay was consistent with that observed in the producer fungus and its mutant where *phm7* was replaced with *fsa2*[19]. Furthermore, there was no significant difference in the amount of *cis*-decalin containing derivative **8** between the presence and absence of enzyme. The time course of the *in vitro* reaction confirmed the approximately linear formation of product **6** for the first several minutes and no cycloaddition in the absence of enzyme under the conditions tested (Supplementary Fig. 13). These results indicated that products **6** and **7** were exclusively formed by the action of Phm7 and Fsa2, respectively, from the linear polyene substrate present in the fungal cell lysate. Therefore, the *in vitro* assay using the fungal cell lysate allowed us to evaluate the enzyme activities by measuring the products formed.

Using the *in vitro* assay system, site-directed mutagenesis studies of Phm7 and Fsa2 were carried out to validate the substrate binding modes predicted by the MD simulations. The key amino acid residues that interact with the tetramic acid moieties (K356 in Phm7 and N346 in Fsa2), the hydrophobic U-shaped parts (W223 in Phm7 and W216 in Fsa2), and the polyene tails (W342 in Phm7 and W332 in Fsa2) were substituted with Ala, and their enzyme activities were compared with those of the wild-type enzymes. Ala-substitutions of these amino acid residues significantly decreased the enzyme activity *in vitro* (Fig. 4c), indicating that the pocket between the N- and C-domains of Phm7 and Fsa2 was the active site of both enzymes, and the proposed binding modes were reliable.

Next, we focused on Phm7 to demonstrate the binding modes. Additional single Ala-substitutions of the amino acid residues close to the substrate **4** were introduced, and the enzyme assay was performed (Fig. 4c). Ala-substitutions of the residues in proximity to the

tetramic acid moiety of **4** (Supplementary Fig. 11) significantly decreased the enzyme activity (Fig. 4c). In particular, a marked decrease in the activity was observed for the mutations of hydrophilic residues such as D53 and E82, suggesting that the hydrophilic upper side-wall of the pocket (Supplementary Fig. 9) was indeed responsible for trapping the tetramic acid moiety of **4**, as predicted by the MD simulations. It is also expected that the hydrogen bond donations from K356 to the carbonyl oxygen at C1 as well as E51 and N84 to the tetramic acid moiety would activate the dienophile to accelerate the reaction. Ala-substitution at Y178 and W223 also significantly decreased enzyme activity (Fig. 4c). A230, L245, and T247 are located near the substrate but do not interact directly with the substrate in the MD model. Substitution of these residues with smaller ones (L245V and T247A) retained considerable activity, while the substitution with longer and larger ones (A230F and T247F) significantly decreased the activity, probably due to steric clash (Fig. 4c and Supplementary Fig. 14). These results confirmed that the **5**-binding site formed by amino acid restudies, such as Y178, W223, L245, and T247, was the reaction chamber in which the stereospecific [4+2] cycloaddition occurred.

To further validate the enzyme-substrate interactions in Phm7, we examined the effects of Ala-substitutions of Phm7 on phomasetin (**2**) production in the producer fungus, in which *phm7* was deleted and the wild-type and mutant *phm7* were introduced. Several Phm7 mutants, including Y68A and W223A, showed significantly lower **2** production in the fungus (Supplementary Fig. 15). Taken together, in depth analyses of Phm7 mutants using an *in vitro* enzyme assay and *in vivo* production in the producer fungus demonstrated the MD simulation-based binding models and amino acid residues involved in substrate binding.

DFT calculations for the molecular mechanism in the Phm7 pocket

Given that Phm7 promotes the [4+2] cycloaddition of substrate **4** in a stereoselective manner, the detailed molecular mechanism in this event with Phm7 should be of great importance. We focused on how Phm7 can determine the stereoselectivity of the cycloaddition, as well as whether this enzyme can accelerate (i.e., catalyze) the reaction. Based on the results of MD simulations, the structure of **4** seemed to be convergent in the major "folded" conformations in the pocket of Phm7 (Supplementary Fig.8a). The geometry between the dienophile and diene moieties in this "folded" structure seems to be close to the configuration that would afford the decalin scaffold having the same configuration as Phm7 product **6** (Fig. 3c). We investigated the intrinsic stereoselectivity of the uncatalyzed cycloaddition of **4** using density functional theory (DFT) calculations at the M06-2X/6–311+G** (scrf = CPCM, water) level of theory (Fig. 5a). Among the four transition states to give the corresponding decalin derivatives, $\mathbf{TS}_{1a}$, which affords **8**, is located in the lowest energy ($\Delta G^{\ddagger}$ +16.1 kcal/mol) from the linear conformation, whereas $\mathbf{TS}_{1b}$ to produce **6** requires slightly higher activation energy ($\Delta G^{\ddagger}$ +16.5 kcal/mol). The reactions to afford Fsa2 type product **7** and another *cis*-decalin derivative were found to be less feasible *via* $\mathbf{TS}_{1c}$ and $\mathbf{TS}_{1d}$, respectively. These computed results suggested that the cycloaddition reaction without any steric bias should give a mixture of **8** and **6**, while **7** might also be present as a minor component. Thus, the combined experimental and theoretical results revealed that the efficient folding of the substrate in the Phm7 pocket should play a pivotal role as a major determinant of the stereoselectivity by the preorganization of the linear polyene substrate **4** to afford a single stereochemical output.

Next, to gain some insight into the rate acceleration mechanism, we focused on the amino acid residues to support the binding of **4** in the Phm7 pocket. In particular, the polar

amino acid residues to support the tetramic acid moiety at the upper side of the pocket were focused on. Similar to Lewis acid coordination, efficient hydrogen bond donation to the carbonyl group adjacent to the dienophile should lower the lowest unoccupied molecular orbital (LUMO) energy of the dienophile and facilitate Diels-Alder reaction[32]. From this point of view, the amine moiety of K356 is a hydrogen bond donor to the corresponding carbonyl group at the C1 of folded **4** (Fig. 5b). DFT calculations at the same level of theory were performed to track the reaction course of the cycloaddition of **4** with methylamine as the model of the K356 residue. However, no significant acceleration was observed, and the activation barrier for **TS*2b*** was +16.6 kcal/mol from the folded conformation. In fact, an efficient decrease in the LUMO energy was not observed. (–0.90 eV for **TS*1b*** vs –0.95 eV for **TS*2b***) (Fig. 5a,c) Taking a closer look at the binding model, we discerned that the amine moiety of K356 has another hydrogen bond with the carboxy group of E82 to form an ammonium architecture (Fig. 5b). We carried out DFT calculations by incorporating methylamine and acetic acid as a model to reproduce the hydrogen bond network (i.e., **4**-K356-E82)[33]. It provides a tight hydrogen bond on the carbonyl oxygen at the C1 of **4** (1.74 Å) due to the acidified proton of the amine group. Further, since the amine protons became more electron-deficient, the additional formation of a weak hydrogen bond[32] (2.35 Å) with the carbonyl oxygen at C2′ was observed. Threrefore, the dihedral angle of the C1 and C2′ carbonyl groups in **TS*3b*** (25.4°) became much smaller than that of **TS*2b*** (33.9°), making the conjugation between the enone dienophile and tetramic acid moiety more efficient. Thus, both electronic and structural perturbation by the hydrogen bond network offered the lowering effects of LUMO energy to –1.04 eV in **TS*3b***, and the cycloaddition reaction was greatly facilitated by lowering the activation barrier for **TS*3b***. (+14.7 kcal/mol). These results can explain the marked decrease in enzymatic activity by

the mutations of E82 (Fig. 4c). In addition, the reason why the Ala-substitution of K356 did not cause a complete loss of activity may be attributed to the direct incorporation of the carboxy group of E82 in hydrogen bonding with **4**, which was also reproduced by the DFT calculation model (Supplementary Fig. 16). Other crucial hydrogen bonds between the tetramic acid moiety and the amino acids, such as E51 and N84, were computationally found not to lower the LUMO energy level (Supplementary Fig. 17) and should be devoted to the appropriate positioning of substrate **4** in the Phm7 pocket.

In sum, the triad of experiments, MD simulations, and DFT calculations revealed the molecular mechanism in the Phm7 pocket as the catalyst for stereoselective [4+2] cycloaddition, including (i) while the intrinsic selectivity of the cycloaddition of **4** prefers the formation of **8** in the absence of the enzyme, the folding structure in the pocket defines the selective formation of **6**, (ii) the sophisticated hydrogen bond network derived from K356 and E82, namely, Brønsted acid-activated hydrogen bonding catalysis, promotes the cycloaddition event very efficiently, and (iii) some polar amino acid residues guide the substrate to the opportune folding structure.

Discussion

Structural analyses of substrate-free Fsa2 and Phm7, and inhibitor-bound Phm7, in combination with MD simulations, site-directed mutagenesis studies, and DFT calculations, revealed a molecular mechanism by which Phm7 and Fsa2 generate enantiomeric products via [4+2] cycloaddition. Phm7 and Fsa2 were comprised of two domains, each of which possessed a lipocalin-like fold. Unlike canonical lipocalin-fold proteins[28], DSs seemed to lose the ability to bind ligands using the original site. Instead, they had acquired the ability to bind unstable linear polyenoyl tetramic acids using the relatively relaxed cavity

between the two domains, exploiting the weak hydrophobic interactions to hold the flexible ligand in the pocket, and eventually catalyzing the cycloaddition. It is noteworthy that the location of the active site on the enzyme was distinct from those of the other known [4+2] cycloaddition enzymes, which catalyze the reactions within or near the inherent active site[9,11,34-39]. Amino acid sequence conservation also supports the origin of this enzyme family. Although there are several conserved amino acid residues among the DSs whose functions have been characterized (Supplementary Fig. 18), none of which, except for W223 in Phm7, were predicted to be involved in the substrate-enzyme interactions, or tested experimentally. Conserved residues likely play a role in maintaining the enzyme structures rather than catalysis. In contrast, DSs seem to share amino acid distributions in the pockets between the two domains (Supplementary Fig. 19). It is likely that substrates bind to the pocket in a similar way (tetramic acid-front and polyene-back orientation) and stereoselective [4+2] cycloadditions proceed. Recent phylogenetic analysis has suggested that approximately 100 sequences are potentially involved in DP biosynthesis[40]. Therefore, this group of enzymes widely found in Ascomycota fungi would be an attractive target for structure-function relationship studies, providing key structural features to determine the stereoselectivity of these reactions.

The MD simulations showed that the pockets between the N- and C-domains of DSs were large enough to accommodate the substrates in various conformations. The “folded” cluster of substrate **4** contains a dominant pose (80%) having a *s-cis* conformation at C9-C10, which explains the expected decalin configurations (Supplementary Fig. 12a,c). The calculated C-C-C-C dihedral angles along the carbon chain of the dominant pose takes a single orientation at all the rotational bonds, and no pose corresponding to the other possible decalin configurations was observed. This indicates that the Phm7 pocket robustly

regulates the rotation of the substrate to stabilize the folded pose with a specific conformation. On the contrary, substrate **3** shows a rather large variation in folded poses (Supplementary Fig. 12b). This is likely due to the fact that Fsa2 binds the smaller substrate to the larger pocket compared to Phm7 (the pocket size is approximately 150 $Å^3$ larger than that of Phm7, Supplementary Fig. 20). In addition, unlike Phm7, which tightly holds the tetramic acid moiety by multiple hydrogen bonds, there is no hydrophilic amino acid residue in the proximity to the C1 carbonyl, and only N346 is involved in hydrogen bonding with **3**. Fsa2 likely retains the substrate affinity to the enzyme by accommodating various folded conformations including the reactive one and minimizing the entropy loss upon binding. These differences between Phm7 and Fsa2 are reminiscent of alternative views of enzyme catalysis mechanisms: transition state stabilization versus reactant de-stabilization[41,42]. In Phm7, the positioning of polar residues seems crucial for the traditional transition state stabilization, while the lack of those residues in Fsa2 may take an alternative reactant de-stabilization, that is, facilitating the preorganization to the reactive conformation. Further investigation of the molecular mechanism of enzymatic cycloaddition with Fsa2, using a hybrid quantum mechanics (QM) /molecular mechanics (MM) method, is expected to fill in the missing piece of the catalytic mechanisms. Given the structural similarity between Phm7 and Fsa2 and their opposite selectivity in the [4+2] cycloaddition, clarification of the detailed mechanism is of significance and the subject of our ongoing research.

In conclusion, our investigations tightly combining experimental and theoretical approaches have highlighted the distinct molecular mechanisms underlying Phm7- and Fsa2-catalyzed [4+2] cycloaddition reactions. The folding of substrate **4** in the Phm7 pocket and **3** in the Fsa2 pocket obtained by the gREST method based on X-ray crystal structures

displayed stereoselectivity in the construction of decalin scaffolds. The results of site-directed mutagenesis studies and DFT calculations clarified how the hydrophilic amino acid residues in the Phm7 pocket regulate and catalyze the stereoselective cycloaddition event. In addition, this study has raised fascinating questions of the molecular tactics adopted by Fsa2 adopts for further research: what determines the transition state from the flexible folded conformations in the pocket, and how Fsa2 accelerates the [4+2] cycloaddition without effective hydrogen bonding on the dienophile moiety.

Methods

Chemicals. All solvents and reagents were of analytical grade and purchased from commercial sources unless noted otherwise. The small molecules used in MST screening, including 3-aminomethyl-*p*-menthane (**5**), and sinefungin were purchased from Namiki Shoji and Cayman Chemical, respectively.

Expression of Fsa2 and Phm7 in *Escherichia coli*. The ORFs of *fsa2* and *phm7* were amplified by PCR with the genomic DNA of *Fusarium* sp. FN080326[43] and *Pyrenochaetopsis* sp. RK10-F058[44], respectively. The amplified decalin synthase (DS) genes were cloned into the pGEM T-easy vector (Promega) and verified by sequencing. The gene fragments were excised by NdeI-XhoI digestion and ligated to the pET28b(+) vector (Novagen), resulting in pET28b(+)-*fsa2* and -*phm7*. Due to inefficient cleavage and removal of the His-tag at the N-terminus of Fsa2, modified pET28b(+)-*fsa2* lacking a thrombin site and linker peptide was used for crystallization study. The primer pairs used for the amplification are listed in Supplementary Table 1. PCR-based site-directed mutagenesis of the DS genes was performed using the primers listed in Supplementary Table 1. Whole plasmids of the mutant DSs were amplified using pET28b(+)-*fsa2* and -*phm7* as templates, which were digested with DpnI after PCR. The amplified cyclic DNAs were introduced into *E. coli* DH5α, and the mutated plasmids were verified by sequencing.

E. coli BL21 Star™ (DE3) (Invitrogen) cells were transformed with pET28b(+)-*fsa2* and -*phm7*, and then cultured in Terrific broth. Gene expression was induced by the addition of isopropyl-β-D-thiogalactopyranoside (0.5 mM), and further cultured at 30 °C for 6 h. For preparation of selenomethionine (SeMet)-substituted Phm7, *E. coli* B834(DE3) carrying pET28b(+)-*phm7* was cultured at 18 °C for 96 h using the Overnight Express Autoinduction

System 2 (Novagen). Cells expressing the DS were harvested by centrifugation and frozen at −80 °C until use.

Purification of Fsa2 and Phm7. The collected Fsa2 expressing cells were resuspended in buffer A (50 mM Tris-HCl, pH7.5, 200 mM NaCl, 10 %(v/v) glycerol) supplemented with 0.5 mg/mL lysozyme and 5 μg/mL Sm2 nuclease, and disrupted by sonication. After centrifugation at 59,800 *g* at 4 °C for 30 min, supernatants were loaded onto a Ni-NTA agarose column (Qiagen). After washing with buffer A containing imidazole (5 mM) and Tween 20 (0.2 % v/v), the enzyme was eluted with buffer A containing 200 mM imidazole. The eluate was 10-times diluted with buffer B1 (50 mM Tris-HCl, pH 8.0, 10 %(v/v) glycerol, 1 mM DTT) and loaded onto a HiTrapQ column, which was pre-equilibrated with buffer B1. The enzyme was eluted with a 0–0.5 M NaCl gradient. The concentrated fractions containing the enzyme were further purified by Superdex 75 16/600 column. The buffer of the purified enzyme was substituted with buffer C (50 mM Tris-HCl, pH7.5, 200 mM NaCl, 5 mM DTT).

The collected Phm7 expressing cells were resuspended in buffer D (50 mM Tris-HCl pH7.5, 500 mM NaCl, 10 %(v/v) glycerol), and disruption and centrifugation were performed as in Fsa2. The supernatants were loaded onto a Ni-NTA agarose column and washed with buffer D containing imidazole (5 mM) and Tween 20 (0.2%). The column was further washed with buffer D containing 30 mM imidazole, and the enzyme was eluted with buffer D containing 200 mM imidazole. The collected fractions containing the enzyme were concentrated and the His-tag was removed by thrombin digestion in a dialysis tube in buffer E (50 mM Tris-HCl, pH 7.5, 200 mM NaCl, 10 %(v/v) glycerol, 20 mM imidazole). Undigested enzyme and thrombin were removed using Ni-NTA and benzamidine

sepharose 6B columns. The enzyme was further purified using resource Q and superdex75 16/600 columns.

The purified Fsa2 and Phm7 were concentrated to 30 and 15 mg/mL, respectively, in crystallization buffer (50 mM Tris-HCl, pH7.5, 200 mM NaCl, 5 mM dithiothreitol) using a 10 kDa cut-off Amicon Ultra-15 concentrator (Merck), and frozen at -80 °C until use.

Phm7 ligand screening using MST assay. To bypass the unavailability of the Phm7 substrate and cofactor for structural studies, ligand screening was conducted using microscale thermophoresis (MST) assay[29]. Fluorescent dye-labeled Phm7 and Fsa2 were prepared using the Monolith Protein labeling kit RED-NHS 2nd generation and Monolith His-Tag Labeling Kit RED-tris-NTA 2G, respectively. MST measurements were performed using a Monolith NT.115 instrument (NanoTemper). In brief, each compound was twofold serially diluted and mixed with equal amounts of the labeled Phm7 (20 nM in 50 mM Tris-HCl, pH 8, 0.15 M NaCl, 10 mM $MgCl_2$, 0.05% Tween20) or Fsa2 (100 nM in 50 mM Tris-HCl, pH 8, 0.2 M NaCl, 0.05% Tween20). After a short incubation, the compound-enzyme mixtures were loaded into glass capillaries and measured for initial fluorescence and change in fluorescence upon thermophoresis measurement. The data were analyzed using the MO Affinity software.

Crystallization of substrate-free Phm7 and Fsa2. Crystallization of the substrate-free forms of Phm7 and Fsa2 and SeMet-substituted Phm7 was performed by mixing 1 μL of the substrate-free enzyme solution with 1 μL of the reservoir solution using the sitting drop vapor diffusion method at 20 °C. Reservoir components for Phm7 were 0.10 M Tris-HCl, pH7.0, 1.56-1.59 M ammonium sulfate, and 15-19 %(v/v) glycerol. For Fsa2, reservoir

solution containing 0.10 M Bis-Tris-HCl, pH7.0, and 26-29 %(w/v) polyethylene glycol 3,350 was used. Initially, small Phm7 multi-crystals were obtained, and 2–6 months were required to obtain large crystals suitable for data collection. Three-dimensional rhombus-shaped single crystals of Fsa2 were obtained within a week. Crystals of SeMet-substituted Phm7 were obtained by the same procedure used for the native Phm7 crystals.

Crystallization of inhibitor 5-bound Phm7. 5-bound Phm7 crystals were prepared by soaking substrate-free crystals in buffer containing 20 mM Tris-HCl pH7.0, 50 mM NaCl, 1.60 M ammonium sulfate, 10 %(v/v) glycerol, 10 mM **5**, 10 %(v/v) ethanol, and 10 %(v/v) dimethyl sulfoxide) for 1 h at 4 ºC.

Data collection and structural determination of Phm7 and Fsa2. All crystals were flash frozen in a cryo-stream at 100 K, and then the crystals were transferred into liquid nitrogen. Prior to flash freezing, Fsa2 crystals in a loop were kept in air for 5–10 s to reduce the water content to prevent damage by buffer replacements. Crystals of a substrate-free and SeMet-substituted Phm7 were soaked in cryo-buffer A; 20 mM Tris-HCl pH7.0, 0.1 M NaCl, 2.0 M ammonium sulfate, 20 %(v/v) glycerol for a few minutes, and crystals of **5**-bound Phm7 were soaked in cryo-buffer B; 50 mM Tris-HCl pH7.0, 2.0 M ammonium sulfate, 20 %(v/v) glycerol, 2.5 mM **5**, 2.5 %(v/v) dimethyl sulfoxide, 7.5 %(v/v) ethanol for a few minutes.

X-ray diffraction data were collected at SPring-8 beamlines BL26B1, BL32XU, BL41XU (Hyogo, Japan), or a Photon Factory beamline BL1A (Ibaraki, Japan). The collected data were integrated and reduced using the XDS package, or AIMLESS from the CCP4 package.

Single-wavelength anomalous diffraction datasets of SeMet-substituted Phm7 crystals were collected at the wavelength of the absorption peak of the selenium atom (0.97920 Å). Substructure determination, phase calculation, and auto model building were performed using Phaser SAD pipeline from the CCP4 package. Three Phm7 molecules were found in the asymmetric unit, and a model of 380 out of 1158 residues were built. Manual model building was performed using Coot, and Refmac5 from CCP4 and Phenix refine were used for structure refinement. We solved the crystal structures of substrate-free Phm7, **5**-bound Phm7, and substrate-free Fsa2 by the molecular replacement method using SeMet-substituted Phm7 as a search model. Data collection and refinement statistics are summarized in Supplementary Table 2. Polder maps of **5** were calculated using Phenix (Supplementary Fig. 21).

Substrate docking simulation. Structural models of polyenoyl tetramic acids **3** and **4** were built and energy minimized using Chem3D v.16.0 (Perkin Elmer). The terminal region of polyenes, which are not involved in [4+2] cycloaddition, was partially restrained by AutoDockTools (v.1.5.6) to maintain the planarity of the C-C double bond. All molecules in the asymmetric unit of the inhibitor-bound Phm7 and the substrate-free Fsa2 crystals were used as receptors, and hydrogen atoms were added to the receptors. Side chains of E82, W223, and K356 of Phm7 were treated as flexible entities to facilitate the calculation, and Fsa2 was treated as a rigid model. The docking simulations were performed using AutoDock Vina under the following conditions: calculation grid boxes for Phm7 and Fsa2 were 44×52×40 and 34×40×38 $Å^3$, and the exhaustiveness values were 150 and 100–200, respectively.

Molecular dynamics (MD) simulations. The initial configurations of protein-ligand complexes, **4**•Phm7 and **3**•Fsa2, were built based on the results of precedent docking simulations using AutoDock Vina. After manual adjustments, each system was neutralized and solvated in 150 mM NaCl solution. All simulations were performed using the GENESIS program package (version 1.4.0)[45,46]. The AMBER ff14SB force field[47] was used for protein and ions, while the TIP3P model[48] was used for water molecules. The ligands were parameterized with the general AMBER force field parameter set version 2.1 (GAFF2) and AM1-BCC atomic charges using the antechamber module in Amber Tools 18[49,50].

gREST simulations. We defined the solute region as the dihedral angle and non-bonded energy (Coulomb and Lennard-Jones) terms of a set of selected binding site residues: D53, S66, Y68, E82, W223, W342, and K356 for Phm7 and the corresponding residues of Fsa2 (D51, G64, T66, Q80, W216, W332, and N346). Eight replicas were employed to cover the solute temperature range of 310.0–773.9 K (T = 310.0, 350.8, 396.7, 452.8, 519.6, 592.3, 675.0, and 773.9 K). We applied a flat-bottom potential to avoid the ligand being away from the binding site.

$$U(R) = \begin{cases} K(R - R_0)^2, R > R_0 \\ 0 \qquad\qquad , R \leq R_0 \end{cases}$$

where R, R_0, and K are the distances between the center of masses of the ligand and binding site residues in the solute region, the flat-bottom distance, and the force constant, respectively. We set R_0 to 15.0 Å and K to 1 kcal/mol/Å^2. The ligand feels no extra force in the region of R = 0–15 Å, while the harmonic restraint potential is applied beyond R = 15 Å to avoid ligand dissociation. Each of the **4**•Phm7 and **3**•Fsa2 systems was initially relaxed at different temperatures for 1 ns followed by production runs for 100 ns per replica (total sampling of 0.8 μs = 100 ns × 8 replicas). The trajectories at 310 K were used for the

analysis. Additional details are provided in the Supplementary Notes.

In vitro enzyme assay. The Δ*phm7* mutant derived from the **2** producer fungus *Pyrenochaetopsis* sp. RK10-F058[19] was cultured at 28 °C for 3 days in Czapek yeast autolysate (CYA) medium[51]. Mycelia were collected, washed, and frozen until use. The mycelia were ground to a fine powder under liquid nitrogen, and approximately 0.1 g of mycelial powder was suspended in 650 μL of extraction buffer (20 mM Tris-HCl, pH 7.5, 10 mM NaCl, 10 mM EDTA, 1% v/v Tween20, 45 μM tetracycline, 200 μM sinefungin). After centrifugation at 20,000 × *g* at 4 °C for 5 min, clear, **4**-saturated supernatants were used as substrate for the *in vitro* enzyme assay. Tetracycline, which was used as an external standard to normalize peak areas, was confirmed to have no effect on the *in vitro* enzyme assay system. Conversion from **6** to **2**, which was mediated by intrinsic methyltransferase activity in the cell lysate, was completely inhibited by 200 μM sinefungin under the conditions tested.

Ten microliters of Phm7 or Fsa2 was added to 30 μL of the substrate and incubated at 25 °C. For evaluation of mutant Phm7 and Fsa2 activities, 100 ng of Phm7 and 10 μg of Fsa2 were used for the reactions, and incubated for 8 and 60 min, respectively. The enzyme reactions were terminated by adding 80 μL of ice-cold MeCN, followed by rapid quenching using liquid nitrogen. The reaction mixtures were thawed, centrifuged, and analyzed by LC/ESI-MS using a Waters Acquity UPLC H-Class system fitted with a mass spectrometer (QDa, Waters). Comparison with authentic standards[19] identified compounds corresponding to peaks **6**, **7**, and **8** as *N*-demethylphomasetin and its derivatives containing **1**-type *trans*- and *cis*-decalin, respectively (Figs. 1b, 4b). An *m*/*z* value of 398.2334 $[M–H]^–$, which was same as that of **6**–**8**, and a characteristic UV spectrum (λ_{max} 293, 305, 319 nm)

for a tetraene substructure suggested the structure of linear pentanenoyl tetramic acid **4** as proposed, although it was too unstable to isolate and determine the structure by NMR.

The LC conditions were as follows: column, Waters Acquity UPLC BEH C18 (2.1×100 mm, 1.7 μm); flow rate, 0.25 mL/min; solvent A, water containing 0.05% (v/v) aqueous formic acid; solvent B, acetonitrile containing 0.05% (v/v) aqueous formic acid. After injection of the samples into a column equilibrated with 5% solvent B, the column was developed with a linear gradient from 5% to 60% solvent B over 1 min and 60% to 100% over 4 min, followed by isocratic elution of 100% solvent B for 6 min.

Characterization of the mutated Phm7 in the producer fungus. The *phm7* gene on the chromosome of the **2** producer fungus *Pyrenochaetopsis* sp. RK10-F058 was replaced with the mutated *phm7* gene under the control of a forced expression promoter (P_{tef1}). Mutations were introduced into pBI121 containing the *ble*-P_{tef1}-*phm7* cassette[19] by PCR-based method as described above. Primer pairs used are listed in Supplementary Table 1. The strain RK10-F058 was transformed with the plasmid carrying the mutated *phm7* using *Agrobacterium tumefaciens*-mediated transformation, and transformants were isolated as described previously[19,52]. Correct replacements and introduced mutations were confirmed by PCR and direct sequencing. Metabolite production of the transformations carrying the mutated *phm7* was analyzed by LC/MS as described previously[19].

DFT calculations. All calculations were carried out with the Gaussian 16 (revision B.01) program package[53]. The molecular structures and harmonic vibrational frequencies were obtained using the hybrid density functional method based on the M06-2X functional[54]. We used the 6-311+G** basis set[55]. The self-consistent reaction field (SCRF) method based on

the conductor-like polarizable continuum model (CPCM)[56-59] was employed to evaluate the solvent reaction field (water; ε = 78.39). Geometry optimization and vibrational analysis were performed at the same level. All stationary points were optimized without any symmetry assumptions and characterized by normal coordinate analysis at the same level of theory (number of imaginary frequencies, NIMAG, 0 for minima and 1 for TSs). The intrinsic reaction coordinate (IRC) method[60,61] was used to track minimum energy paths from transition structures to the corresponding local minima.

Acknowledgements

We acknowledge the computational resources provided by the RIKEN Advanced Center for Computing and Communication (HOKUSAI GreatWave and BigWaterfall) and the HPCI system (Project ID: hp200153) for the MD simulations and the Research Center for Computational Science (Okazaki, Japan) for the DFT calculations. This work was supported by MEXT/KAKENHI (Grant Numbers 19H04665, 20K05872 (to NK), 19K12229 (to SR), 19K06992 (to RT), 20K15273 (to KW), 19H05645 (to YS), 19H04658, 19H05780 (to SN)), MEXT as “Priority Issue on Post-K computer” (Building Innovative Drug Discovery Infrastructure Through Functional Control of Biomolecular Systems), the Takeda Science Foundation (to RT), and the Naito Foundation (to RT), and RIKEN Pioneering Research Projects (Dynamic Structural Biology/Glycolipidologue Initiative) (to YS).

References

1. Pasteur, L. Sur les relations qui peuvent exister entre la forme crystalline, la composition chimique et le sens de la polarization rotatoire. *Annales Chimie Phys.* **24**, 442-459 (1848).
2. Minami, A. & Oikawa, H. Recent advances of Diels-Alderases involved in natural product biosynthesis. *J Antibiot* **69**, 500-506 (2016).

3. Jeon, B.S., Wang, S.A., Ruszczycky, M.W. & Liu, H.W. Natural [4 + 2]-cyclases. *Chem Rev* **117**, 5367-5388 (2017).
4. Jamieson, C.S., Ohashi, M., Liu, F., Tang, Y. & Houk, K.N. The expanding world of biosynthetic pericyclases: cooperation of experiment and theory for discovery. *Nat Prod Rep* **36**, 698-713 (2019).
5. Lichman, B.R., O'Connor, S.E. & Kries, H. Biocatalytic strategies towards [4+2] cycloadditions. *Chemistry* **25**, 6864-6877 (2019).
6. Kim, H.J., Ruszczycky, M.W., Choi, S.H., Liu, Y.N. & Liu, H.W. Enzyme-catalysed [4+2] cycloaddition is a key step in the biosynthesis of spinosyn A. *Nature* **473**, 109-112 (2011).
7. Fischbach, M.A. & Walsh, C.T. Assembly-line enzymology for polyketide and nonribosomal peptide antibiotics: logic, machinery, and mechanisms. *Chem Rev* **106**, 3468-3496 (2006).
8. Gao, Y., Honzatko, R.B. & Peters, R.J. Terpenoid synthase structures: a so far incomplete view of complex catalysis. *Nat Prod Rep* **29**, 1153-1175 (2012).
9. Fage, C.D. et al. The structure of SpnF, a standalone enzyme that catalyzes [4 + 2] cycloaddition. *Nat Chem Biol* **11**, 256-258 (2015).
10. Tian, Z. et al. An enzymatic [4+2] cyclization cascade creates the pentacyclic core of pyrroindomycins. *Nat Chem Biol* **11**, 259-265 (2015).
11. Zheng, Q. et al. Structural insights into a flavin-dependent [4 + 2] cyclase that catalyzes *trans*-decalin formation in pyrroindomycin biosynthesis. *Cell Chem Biol* **25**, 718-727 e3 (2018).
12. Kato, N. et al. A new enzyme involved in the control of the stereochemistry in the decalin formation during equisetin biosynthesis. *Biochem Biophys Res Commun* **460**, 210-215 (2015).
13. Schobert, R. & Schlenk, A. Tetramic and tetronic acids: an update on new derivatives and biological aspects. *Bioorg Med Chem* **16**, 4203-4221 (2008).
14. Li, G., Kusari, S. & Spiteller, M. Natural products containing 'decalin' motif in microorganisms. *Nat Prod Rep* **31**, 1175-1201 (2014).
15. Burmeister, H.R., Bennett, G.A., Vesonder, R.F. & Hesseltine, C.W. Antibiotic produced by *Fusarium equiseti* NRRL 5537. *Antimicrob Agents Chemother* **5**, 634-639 (1974).
16. Singh, S.B. et al. Equisetin and a novel opposite stereochemical homolog phomasetin, two fungal metabolites as inhibitors of HIV-1 integrase. *Tetrahedron Lett* **39**, 2243-2246 (1998).
17. Agatsuma, T. et al. UCS1025A and B, new antitumor antibiotics from the fungus *Acremonium* species. *Org Lett* **4**, 4387-4390 (2002).
18. Nakai, R. et al. Telomerase inhibitors identified by a forward chemical genetics approach

using a yeast strain with shortened telomere length. *Chem Biol* **13**, 183-190 (2006).

19. Kato, N. et al. Control of the stereochemical course of [4+2] cycloaddition during *trans*-decalin formation by Fsa2-family enzymes. *Angew Chem Int Ed Engl* **57**, 9754-9758 (2018).
20. Li, X., Zheng, Q., Yin, J., Liu, W. & Gao, S. Chemo-enzymatic synthesis of equisetin. *Chem Commun* **53**, 4695-4697 (2017).
21. Li, L. et al. Biochemical characterization of a eukaryotic decalin-forming Diels-Alderase. *J Am Chem Soc* **138**, 15837-15840 (2016).
22. Sato, M. et al. Involvement of lipocalin-like CghA in decalin-forming stereoselective intramolecular [4+2] cycloaddition. *Chembiochem* **16**, 2294-2298 (2015).
23. Li, L. et al. Genome mining and assembly-line biosynthesis of the UCS1025A pyrrolizidinone family of fungal alkaloids. *J Am Chem Soc* **140**, 2067-2071 (2018).
24. Tan, D. et al. Genome-mined Diels-Alderase catalyzes formation of the *cis*-octahydrodecalins of varicidin A and B. *J Am Chem Soc* **141**, 769-773 (2019).
25. Kamiya, M. & Sugita, Y. Flexible selection of the solute region in replica exchange with solute tempering: Application to protein-folding simulations. *J Chem Phys* **149**, 072304 (2018).
26. Re, S., Oshima, H., Kasahara, K., Kamiya, M. & Sugita, Y. Encounter complexes and hidden poses of kinase-inhibitor binding on the free-energy landscape. *Proc Natl Acad Sci U S A* **116**, 18404-18409 (2019).
27. Niitsu, A., Re, S., Oshima, H., Kamiya, M. & Sugita, Y. De novo prediction of binders and nonbinders for T4 lysozyme by gREST simulations. *J Chem Inf Model* **59**, 3879-3888 (2019).
28. Flower, D.R., North, A.C. & Sansom, C.E. The lipocalin protein family: structural and sequence overview. *Biochim Biophys Acta* **1482**, 9-24 (2000).
29. Wienken, C.J., Baaske, P., Rothbauer, U., Braun, D. & Duhr, S. Protein-binding assays in biological liquids using microscale thermophoresis. *Nat Commun* **1**, 100 (2010).
30. Allouche, A.R. Gabedit--a graphical user interface for computational chemistry softwares. *J Comput Chem* **32**, 174-182 (2011).
31. Wallace, A.C., Laskowski, R.A. & Thornton, J.M. LIGPLOT: a program to generate schematic diagrams of protein-ligand interactions. *Protein Eng* **8**, 127-134 (1995).
32. Taylor, M.S. & Jacobsen, E.N. Asymmetric catalysis by chiral hydrogen-bond donors. *Angew Chem Int Ed Engl* **45**, 1520-1543 (2006).
33. Zou, Y. et al. Computational investigation of the mechanism of Diels-Alderase PyrI4. *J Am Chem Soc* **142**, 20232-20239 (2020).
34. Zheng, Q. et al. Enzyme-dependent [4 + 2] cycloaddition depends on lid-like interaction

of the N-terminal sequence with the catalytic core in PyrI4. *Cell Chem Biol* **23**, 352-360 (2016).

35. Byrne, M.J. et al. The Catalytic mechanism of a natural Diels-Alderase revealed in molecular detail. *J Am Chem Soc* **138**, 6095-6098 (2016).
36. Cogan, D.P. et al. Structural insights into enzymatic [4+2] aza-cycloaddition in thiopeptide antibiotic biosynthesis. *Proc Natl Acad Sci U S A* **114**, 12928-12933 (2017).
37. Cai, Y. et al. Structural basis for stereoselective dehydration and hydrogen-bonding catalysis by the SAM-dependent pericyclase LepI. *Nat Chem* **11**, 812-820 (2019).
38. Dan, Q. et al. Fungal indole alkaloid biogenesis through evolution of a bifunctional reductase/Diels-Alderase. *Nat Chem* **11**, 972-980 (2019).
39. Gao, L. et al. FAD-dependent enzyme-catalysed intermolecular [4+2] cycloaddition in natural product biosynthesis. *Nat Chem* **12**, 620-628 (2020).
40. Minami, A., Ugai, T., Ozaki, T. & Oikawa, H. Predicting the chemical space of fungal polyketides by phylogeny-based bioinformatics analysis of polyketide synthase-nonribosomal peptide synthetase and its modification enzymes. *Sci Rep* **10**, 13556 (2020).
41. Hur, S. & Bruice, T.C. The near attack conformation approach to the study of the chorismate to prephenate reaction. *Proc Natl Acad Sci U S A* **100**, 12015-12020 (2003).
42. Burschowsky, D. et al. Electrostatic transition state stabilization rather than reactant destabilization provides the chemical basis for efficient chorismate mutase catalysis. *Proc Natl Acad Sci U S A* **111**, 17516-17521 (2014).
43. Jang, J.H. et al. Fusarisetin A, an acinar morphogenesis inhibitor from a soil fungus, *Fusarium* sp. FN080326. *J Am Chem Soc* **133**, 6865-6867 (2011).
44. Nogawa, T. et al. Wakodecalines A and B, new decaline metabolites isolated from a fungus *Pyrenochaetopsis* sp. RK10-F058. *J Antibiot* **71**, 123-128 (2018).
45. Jung, J. et al. GENESIS: a hybrid-parallel and multi-scale molecular dynamics simulator with enhanced sampling algorithms for biomolecular and cellular simulations. *Wiley Interdiscip Rev Comput Mol Sci* **5**, 310-323 (2015).
46. Kobayashi, C. et al. GENESIS 1.1: A hybrid-parallel molecular dynamics simulator with enhanced sampling algorithms on multiple computational platforms. *J Comput Chem* **38**, 2193-2206 (2017).
47. Maier, J.A. et al. ff14SB: Improving the accuracy of protein side chain and backbone parameters from ff99SB. *J Chem Theory Comput* **11**, 3696-3713 (2015).
48. Jorgensen, W.L., Chandrasekhar, J., Madura, J.D., Impey, R.W. & Klein, M.L. Comparison of simple potential functions for simulating liquid water. *J Chem Phys* **79**, 926-935 (1983).

49. Wang, J., Wolf, R.M., Caldwell, J.W., Kollman, P.A. & Case, D.A. Development and testing of a general amber force field. *J Comput Chem* **25**, 1157-1174 (2004).
50. Case, D.A. et al. AMBER 2018. *University of California, San Francisco.* (2018).
51. Frisvad, J.C. Media and growth conditions for induction of secondary metabolite production. *Methods Mol Biol* **944**, 47-58 (2012).
52. Motoyama, T., Hayashi, T., Hirota, H., Ueki, M. & Osada, H. Terpendole E, a kinesin Eg5 inhibitor, is a key biosynthetic intermediate of indole-diterpenes in the producing fungus *Chaunopycnis alba*. *Chem Biol* **19**, 1611-1619 (2012).
53. Frisch, M.J. et al. Gaussian 16 Rev. B.01. (Wallingford, CT, 2016).
54. Zhao, Y. & Truhlar, D.G. The M06 suite of density functionals for main group thermochemistry, thermochemical kinetics, noncovalent interactions, excited states, and transition elements: two new functionals and systematic testing of four M06-class functionals and 12 other functionals. *Theor Chem Account* **120**, 215-241 (2008).
55. Frisch, M.J., Pople, J.A. & Binkley, J.S. Self-consistent molecular orbital methods 25. Supplementary functions for Gaussian basis sets. *J Chem Phys* **80**, 3265-3269 (1984).
56. Klamt, A. & Schuurmann, G. COSMO: a new approach to dielectric screening in solvents with explicit expressions for the screening energy and its gradient. *J Chem Soc, Perkin Trans 2*, 799-805 (1993).
57. Andzelm, J., Kölmel, C. & Klamt, A. Incorporation of solvent effects into density functional calculations of molecular energies and geometries. *J Chem Phys* **103**, 9312-9320 (1995).
58. Barone, V. & Cossi, M. Quantum Calculation of Molecular Energies and Energy Gradients in Solution by a Conductor Solvent Model. *J Phys Chem A* **102**, 1995-2001 (1998).
59. Cossi, M., Rega, N., Scalmani, G. & Barone, V. Energies, structures, and electronic properties of molecules in solution with the C-PCM solvation model. *J Comput Chem* **24**, 669-681 (2003).
60. Ishida, K., Morokuma, K. & Komornicki, A. The intrinsic reaction coordinate. An *ab initio* calculation for HNC→HCN and $H^- + CH_4 \rightarrow CH_4 + H^-$ *J Chem Phys* **66**, 2153-2156 (1977).
61. Fukui, K. The path of chemical reactions - the IRC approach. *Acc Chem Res* **14**, 363-368 (1981).

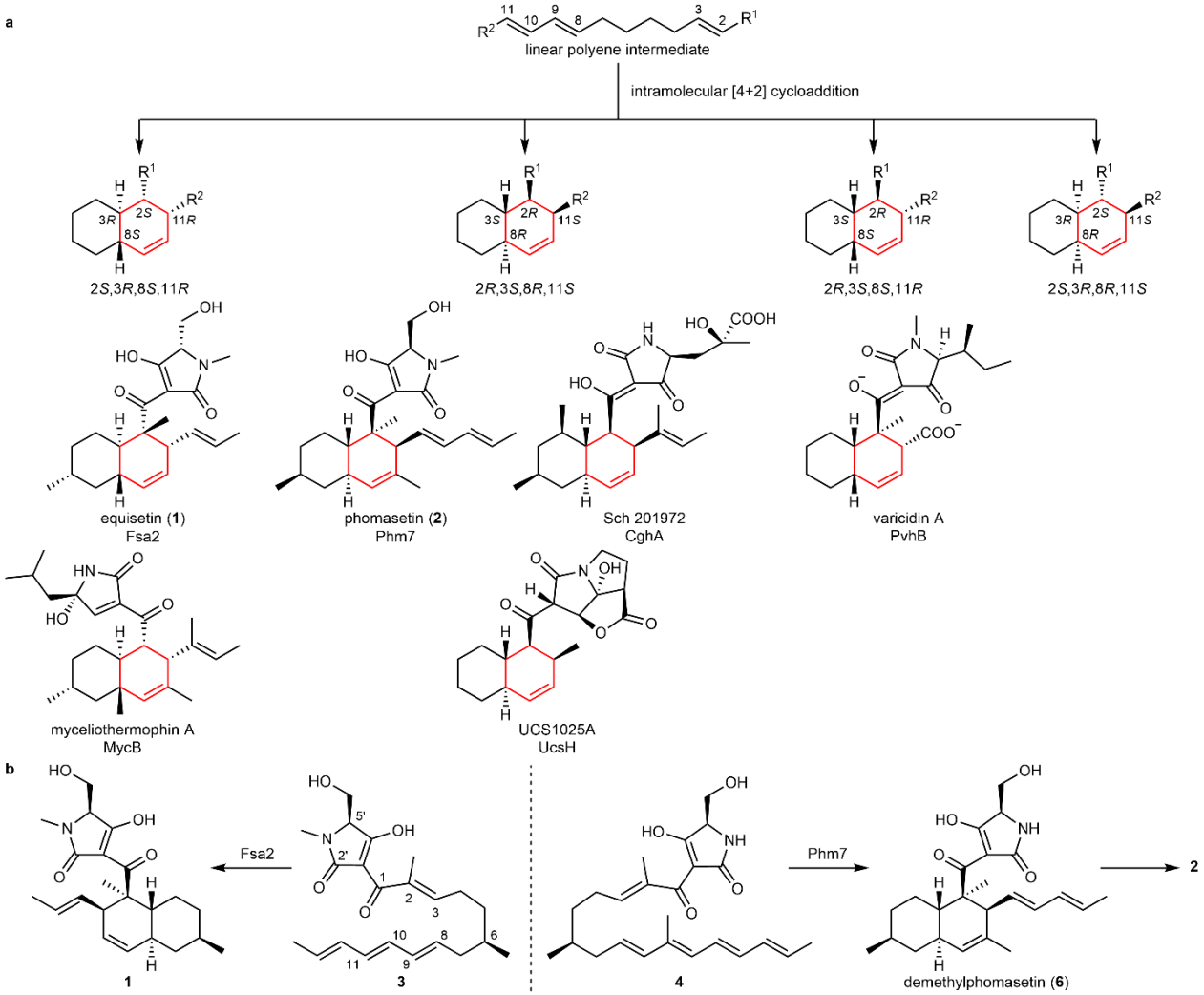

Fig. 1: The Fsa2-family decalin synthases (DSs) catalyzing stereoselective [4+2] cycloaddition. a, Four possible configurations of decalin formed via intramolecular [4+2] cycloaddition, and corresponding Fsa2-family DSs. **b**, The reactions catalyzed by Fsa2 and Phm7 to form enantiomeric decalin scaffolds. Linear tetraenoyl tetramic acid **3** was chemically synthesized and confirmed to be a Fsa2 substrate to form **1**[20], whereas pentaenoyl tetramic acid **4** is a likely Phm7 substrate to yield *N*-demethylphomasetin (**6**), which is further converted to **2**.

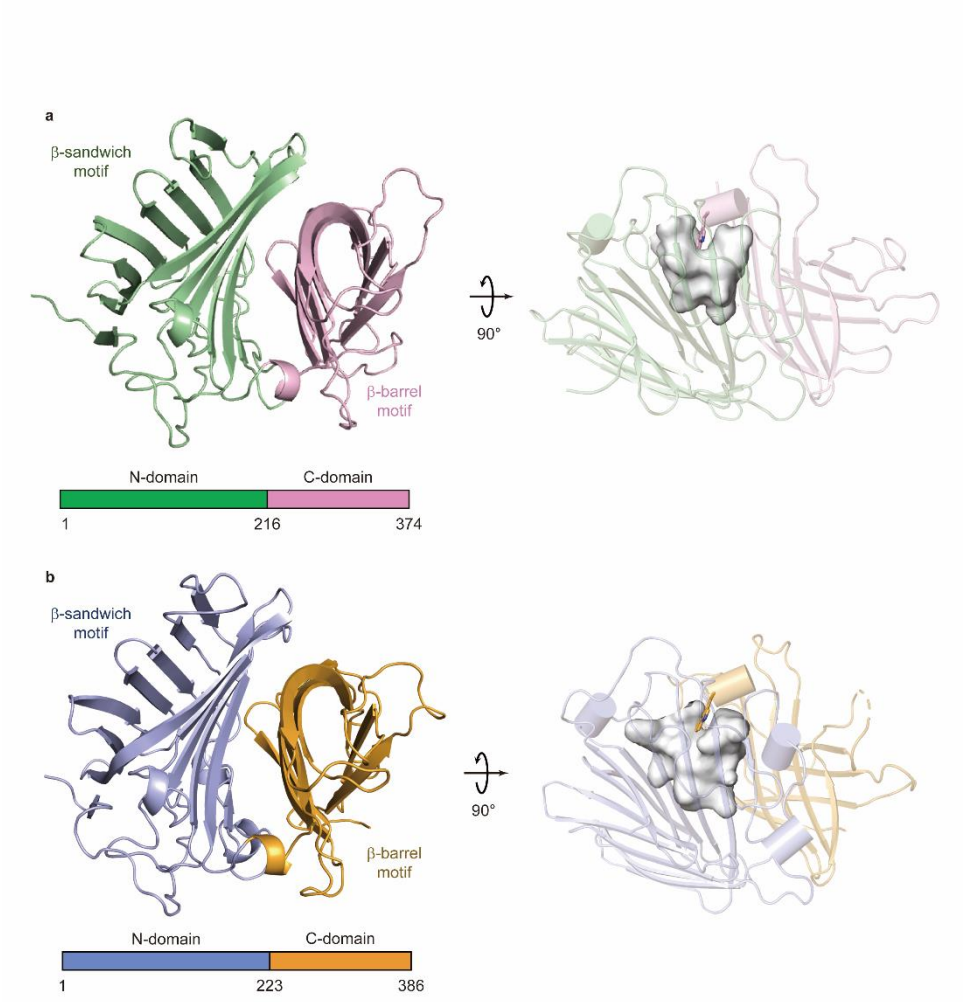

Fig. 2: Crystal structures of Fsa2 and Phm7. a,b, Overall structures of Fsa2 (**a**) and Phm7 (**b**). Both DSs consist of two domains: N-domains for residues 1-215 of Fsa2 and 1-222 of Phm7, and C-domains for residues 216-374 and 223-386. Surface models (right panels) show shapes of the pocket between the two domains of both enzymes.

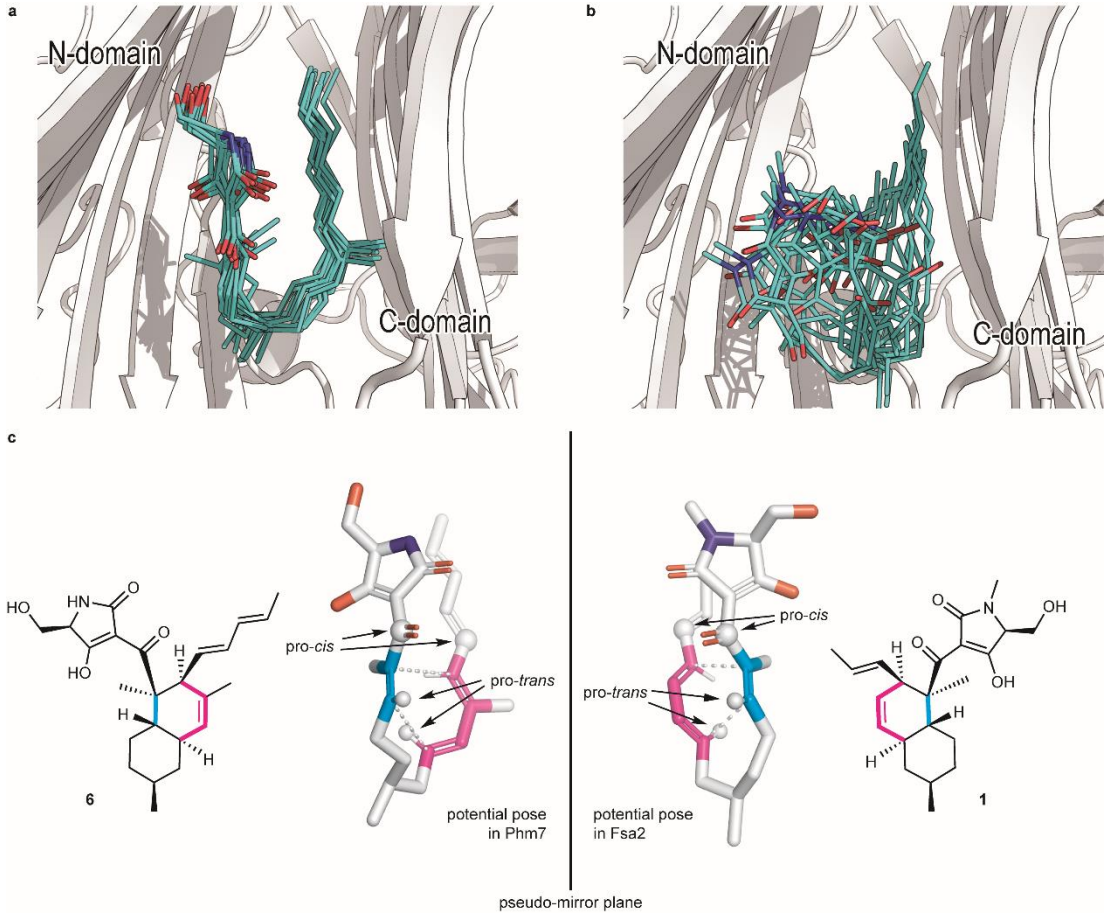

Fig. 3: Predicted binding model. a, **b**, A collective view of 12 representative snapshots taken from the top 70% of the main folded clusters (chosen based on the RMSD values from the cluster center in ascending order) for Phm7 (**a**) and Fsa2 **(b**), respectively. **c**, Conformations of the major poses of **4** (left) and **3** (right) in the pockets. The diene and dienophile moieties of the substrate are indicated in pink and cyan, respectively. The corresponding cycloadducts are also shown.

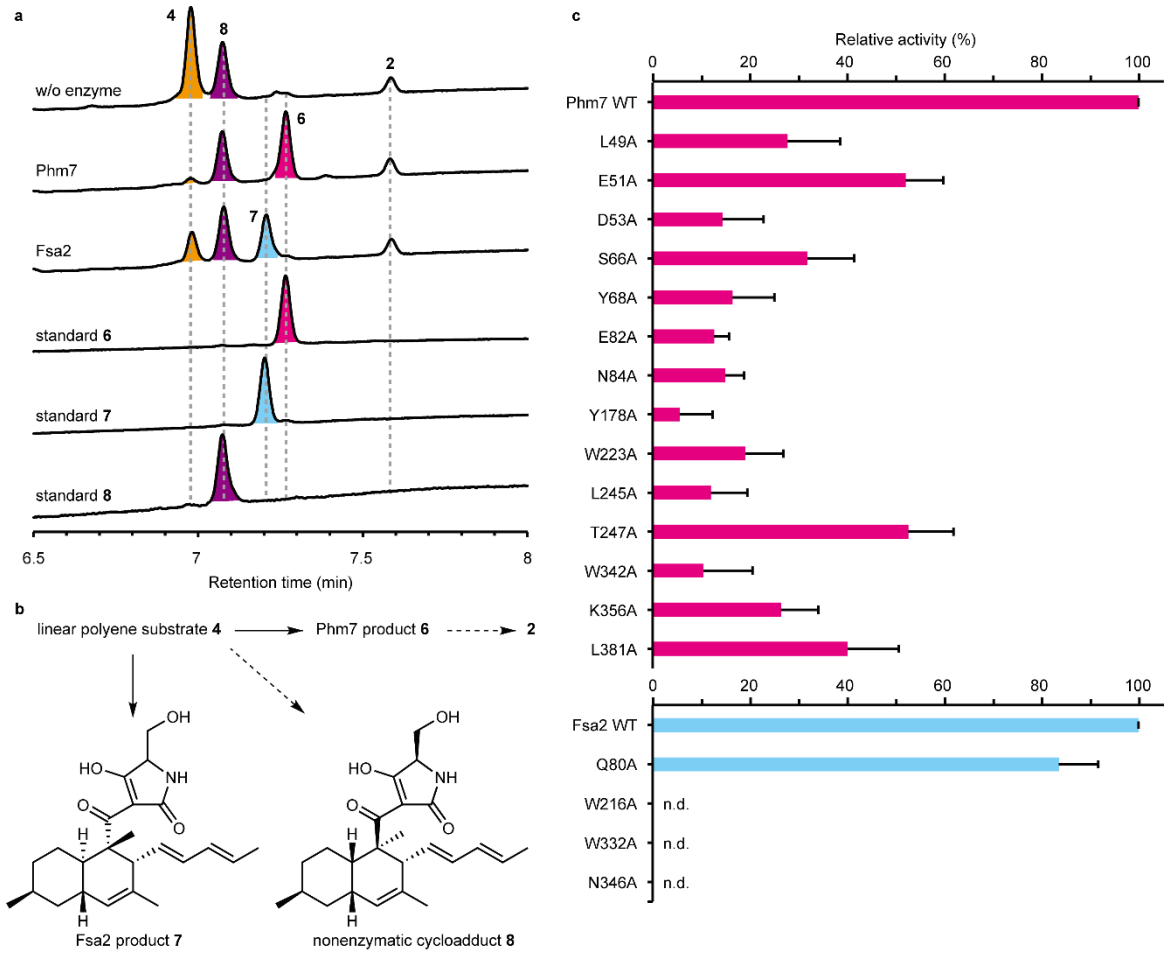

Fig. 4: In vitro analysis of Ala-substituted Phm7 and Fsa2 mutants. a, UPLC traces of the *in vitro* Phm7 and Fsa2 reaction products. The cell lysates prepared from the Δ*phm7* mycelia were incubated with Phm7 and Fsa2 and analyzed by LC/ESI-MS. **b**, Linear polyenoyl tetramic acid **4** was converted into **6** and **7** by Phm7 and Fsa2, respectively. Conversions indicated by broken arrows were not detected under the conditions tested: non-enzymatic formation of **8** from **4** was not observed *in vitro*, and sinefungin added in the reaction buffer inhibited *N*-methylation of **6**. **c**, Comparison of the enzyme activities of the Ala-substituted mutants with those of the wild-type Phm7 and Fsa2. Data are the mean and error bars represent the standard deviation of four independent experiments. n.d, not detected.

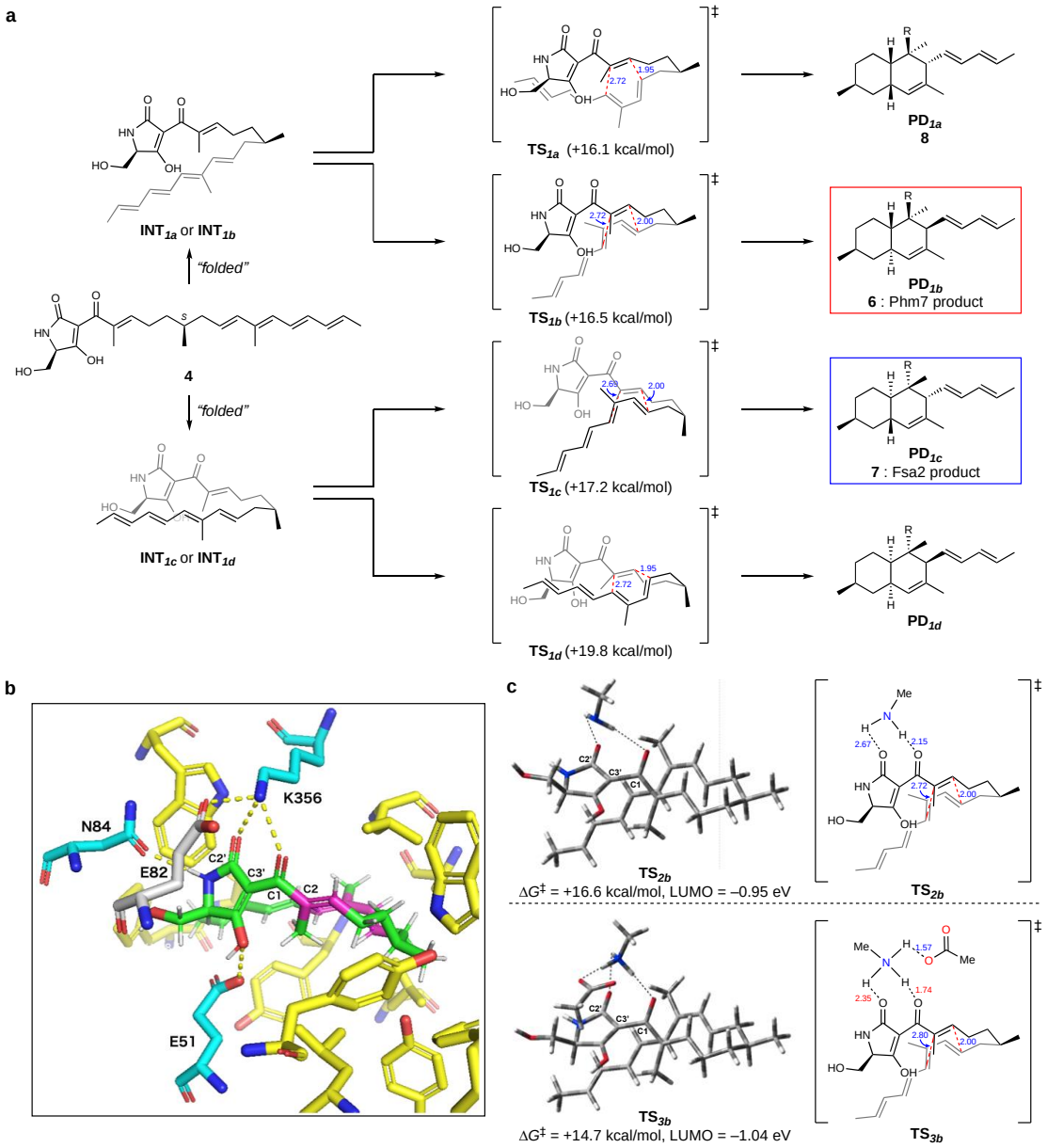

Fig. 5: The DFT calculations for the reaction mechanism of the uncatalyzed and hydrogen bond-catalyzed cycloaddition of 4. a, Reaction pathways for the uncatalyzed cycloaddition of substrate **4** to produce four types of decalin stereoisomers. The energy changes and bond lengths were calculated at the M06-2X/6-311+G** (scrf = CPCM, water) level of theory are shown in kcal/mol and Å, respectively. **b**, Illustration of the hydrogen bond network of **4** with amino acid residues in the Phm7 pocket obtained from the MD simulation (cf. Supplementary Fig. 11a). **c**, Transition state structures to give **6** with methylamine (**TS*2b***) and both methylamine and acetic acid (**TS*3b***) as the models for the hydrogen bonding with K356 and E82 residues.